Nanoscale

PAPER

Cite this: *Nanoscale*, 2018, **10**, 23087

Measurement of the thermal conductivities of suspended MoS_2 and $MoSe_2$ by nanosecond ET-Raman without temperature calibration and laser absorption evaluation

Ridong Wang,[a] Tianyu Wang,[a] Hamidreza Zobeiri,[a] Pengyu Yuan,[b] Cheng Deng,[c] Yanan Yue,[d] Shen Xu*[e] and Xinwei Wang*[a]

Received 13th July 2018,
Accepted 12th November 2018

DOI: 10.1039/c8nr05641b

rsc.li/nanoscale

Steady state Raman spectroscopy is the most widely used opto-thermal technique for measuring a 2D atomic-layer material's thermal conductivity. It requires the calibration of temperature coefficients of Raman properties and measurement/calculation of the absolution laser absorption in 2D materials. Such a requirement is very laborious and introduces very large measurement errors (of the order of 100%) and hinders gaining a precise and deep understanding of phonon–structure interactions in 2D materials. In this work, a novel nanosecond energy transport state resolved Raman (ns ET-Raman) technique is developed to resolve these critical issues and achieve unprecedented measurement precision, accuracy and ease of implementation. In ns ET-Raman, two energy transport states are constructed: steady state and nanosecond thermal transport and Raman probing. The ratio of the temperature rise under the two states eliminates the need for Raman temperature calibration and laser absorption evaluation. Four suspended MoS_2 (45–115 nm thick) and four suspended $MoSe_2$ (45–140 nm thick) samples are measured and compared using ns ET-Raman. With the increase of the sample thickness, the measured thermal conductivity increases from 40.0 ± 2.2 to 74.3 ± 3.2 W m^{-1} K^{-1} for MoS_2, and from 11.1 ± 0.4 to 20.3 ± 0.9 W m^{-1} K^{-1} for $MoSe_2$. This is attributed to the decreased significance of surface phonon scattering in thicker samples. The ns ET-Raman features the most advanced capability to measure the thermal conductivity of 2D materials and will find broad applications in studying low-dimensional materials.

Introduction

2D atomic-layer materials such as graphene,[1,2] hexagonal boron nitride (h-BN),[3] black phosphorus,[4,5] molybdenum disulfide (MoS_2),[6] and molybdenum diselenide ($MoSe_2$)[7] have attracted significant research attention. One of the reasons for the rapid progress is that these materials are thought to be the most suitable candidate to create a new generation of electronic devices.[8,9] The performance of electronic devices largely relies on the heat dissipation property and hence on the thermal conductivity of the materials.[10] As a result, it is very crucial to measure, understand, and tailor/improve the thermal conductivity of 2D atomic-layer materials.

Some previous studies have reported the thermal conductivity of different 2D atomic-layer materials. Jo *et al.*[11] used a microbridge device with built-in resistance thermometers to measure the thermal conductivity of suspended few-layered hexagonal boron nitride (h-BN). Based on the obtained thermal resistance of the 11-layer h-BN samples with suspended lengths ranging from 3 to 7.5 μm, the in-plane thermal conductivity at room temperature was found to be about 360 W m^{-1} K^{-1}. In this method, the measurement accuracy is jeopardized by the unknown thermal contact resistance between the sample and the contacts. Jang *et al.*[12] measured the thermal conductivity in different directions of mechanically exfoliated black phosphorus (BP) of 138–552 nm thickness using the conventional time-domain thermoreflectance (TDTR) and beam-offset TDTR methods. The highest in-plane thermal conductivities were 86 ± 8 and 34 ± 4 W m^{-1} K^{-1} along the zigzag and the armchair directions, respectively. The cross-plane thermal conductivity was 4.0 ± 0.5 W m^{-1} K^{-1}.

---

[a] *Department of Mechanical Engineering, Iowa State University, Ames, Iowa 50011, USA. E-mail: xwang3@iastate.edu*
[b] *The Molecular Foundry, Lawrence Berkeley National Laboratory, One Cyclotron Road, Building 67, Berkeley, CA 94720, USA*
[c] *College of Mechatronics Engineering, Guangdong Polytechnic Normal University, Guangzhou 510635, People's Republic of China*
[d] *School of Power and Mechanical Engineering, Wuhan University, Wuhan 430072, People's Republic of China*
[e] *Automotive Engineering College, Shanghai University of Engineering Science, 333 Longteng Road, Shanghai 201620, People's Republic of China. E-mail: xx_xs316@163.com*

Compared with other methods, this method requires more complicated setups and very careful operation to obtain data for further analysis.[13] Shahil *et al.*[14] used the transient "laser flash" technique (LFT) to measure the cross-plane thermal conductivity of graphene-based thermal interface materials. Based on the resulting temperature evolution, the thermal diffusivity could be determined. The specific heat of the material could be obtained by comparing the magnitude of the temperature rise to that of the reference calibration sample. Then, the thermal conductivity was calculated by using these two parameters. However, this method cannot be used to measure thin films. Typical commercial laser flash instruments can measure samples with a thickness of ~100 μm or above depending on the thermal diffusivity of the sample.[15]

Among the different methods to measure the thermal properties of 2D atomic-layer materials, an optothermal method based on Raman spectroscopy is the most widely used one.[16] In this method, a laser is focused on a 2D atomic-layer material and the positions of the corresponding Raman-active mode are measured. The laser heating enables Raman redshift due to thermal softening.[17] Thermal modeling can then be used to extract the thermal conductivity from the measured shift rate. Several parameters, such as the rate of mode softening with temperature,[18] optical absorption,[19] 2D atomic layer interface thermal resistance (*R*),[20] and hot carrier diffusion coefficient (*D*),[21] are required to realize the determination of thermal conductivity using thermal modeling. The work of Yuan *et al.*[21] is the first one to consider the energy re-distribution by hot carriers and they were able to measure the hot carrier diffusivity and mobility *via* a completely non-contact way.

As the optothermal method based on Raman spectroscopy is a widely used method, many research groups used this method to measure the thermal conductivity of 2D atomic-layer materials. Lee *et al.*[22] measured the thermal conductivity of suspended pristine graphene over holes with diameter ranging from 2.6 to 6.6 μm. Luo *et al.*[23] reported the anisotropic in-plane thermal conductivity of suspended few-layered BP. Yan *et al.*[24] used this technique to measure the thermal conductivity of suspended monolayer MoS_2 over holes with a diameter of 1.2 μm. Zhang *et al.*[25] used this technique to study the thermal conductivity of monolayer and bilayer MoS_2 and monolayer and bilayer $MoSe_2$. To minimize the effects of the finite spot size, the samples were suspended over holes with diameter between 2.5 and 5 μm.

Though the optothermal method based on Raman spectroscopy has been widely used to measure the thermal conductivity of 2D atomic-layer materials, a significant drawback of this method is that both temperature and power dependent Raman studies should be done to extract the thermal conductivity of the sample. However, the temperature-dependent Raman study is very time consuming and could introduce large errors. Also the laser absorption is subject to very large errors induced by unknown sample-to-sample optical property variations. In our recently published work, we have developed a novel and more advanced technique: energy transport state-resolved Raman (ET-Raman) to study the 2D atomic-layer materials' thermal properties.[26] The error introduced by Raman property temperature coefficient calibration could be eliminated using this technique. The ET-Raman is based on two extreme energy transport situations: near zero transport using a picosecond (ps) laser Raman and steady-state using a continuous-wave (CW) laser Raman. One of the most attractive perspectives is that we do not need to know the laser absorption coefficient or the temperature coefficients of the Raman properties. The hot carrier diffusivity and interface thermal resistance could be determined by just comparing the Raman shift variations measured from different energy transport states in time and space domains. Thus, this technique eliminates the errors brought in by local optical absorption evaluation, temperature coefficient calibration, and the effects from the electrical contact used in carrier mobility measurements. However, this ET-Raman technique with a picosecond laser can only be used for supported materials since the pulse interval is so short that a strong heat accumulation for suspended 2D atomic-layer materials will happen.

In this work, we conduct further development of the ET-Raman technique using a nanosecond (ns) laser for measuring the thermal conductivity of suspended 2D atomic-layer materials. The pulse interval of the ns laser is 10 μs, which is much longer than that of the ps laser (~26 ns). A ns ET-Raman technology is developed to measure the in-plane thermal conductivity of suspended MoS_2 and $MoSe_2$. The thickness effect on in-plane thermal conductivity for these two 2D atomic-layer materials is explored. The thickness of the nanosheets ranges from 45 nm to 115 nm for MoS_2, and from 40 nm to 135 nm for $MoSe_2$.

Results and discussion

ns ET-Raman physics

Although the Raman active optical phonons do not play a significant role in directly conducting heat in the in-plane direction, their frequency of vibration is reasonably sensitive to the local temperature fluctuations caused by external effects.[27] The temperature increase of the suspended sample under laser excitation is directly related to the thermal conductivity of the material.[28] In the ns ET-Raman technique, we construct two distinct energy transport states in the time domain to probe the materials' thermal response. Two lasers with 532 nm wavelength are used to irradiate the samples for both laser heating and Raman probing. Fig. 1(a) shows the suspended sample, and the center of the sample is irradiated by the laser. The first energy transport state is the steady-state heating. As shown in Fig. 1(b) and (c), a CW laser is used to generate steady-state heating, and to explore the temperature profile that depends on thermal conductivity. The MoS_2 or $MoSe_2$ nanosheets will absorb the laser energy and transport it along the in-plane and cross-plane directions. Compared with its lateral size, the thickness of the nanosheets is very small. As a result, the energy transport in the cross-plane direction could

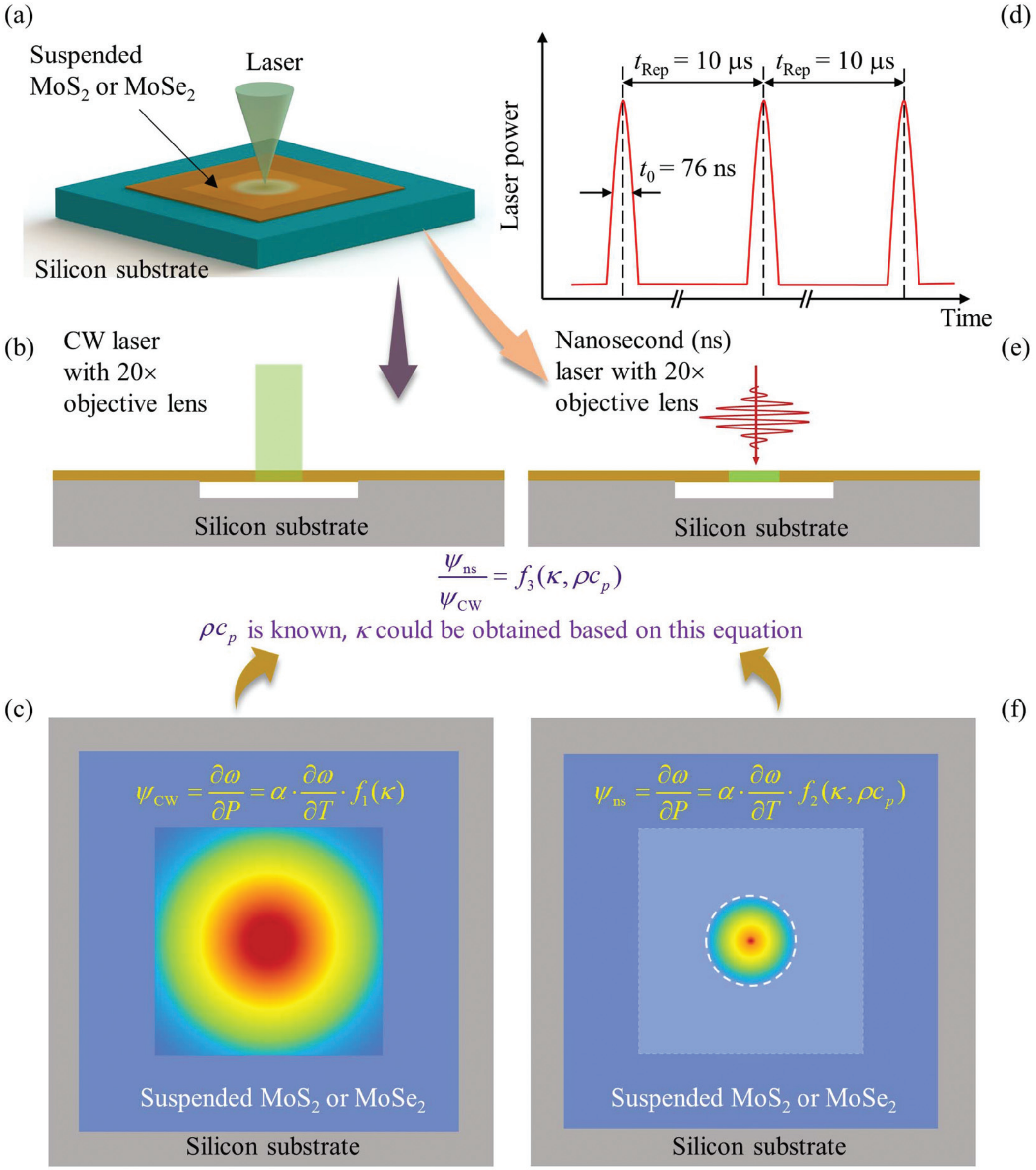

Fig. 1 Illustration of the nanosecond energy transport state resolved Raman (ns ET-Raman) concept. (a) The MoS_2 or $MoSe_2$ nanosheets are transferred to the silicon substrate with a hole beneath. (b)–(f) A 532 nm continuous-wave (CW) laser and a 532 nm nanosecond (ns) laser are used to generate two different energy transport states in the time domain with the same objective lens (20×). Due to the different contributions of in-plane thermal conductivity under the two energy transport states, the in-plane thermal conductivity of the sample could be obtained.

be neglected and the temperature can be treated as a constant in the thickness direction. Raman signal is also excited during the laser heating and could be collected to obtain the temperature profile of the sample. By using different laser powers (P), a parameter called the Raman shift power coefficient (RSC) could be obtained: $\psi_{CW} = \partial\omega/\partial P = \alpha(\partial\omega/\partial T)f_1(\kappa)$. ψ_{CW} is determined by the laser absorption coefficient (α), the temperature coefficient of the Raman shift ($\partial\omega/\partial T$), and the in-plane thermal conductivity of the sample (κ).

The second energy transport state is the opposite of the steady state: it has nearly zero transport. Fig. 1(d) and (e) show that a ns laser is focused in the center of the suspended sample to realize localized heating and Raman probing. In the same way, as shown in Fig. 1(f), the RSC for this ns laser heating case could also be obtained: $\psi_{ns} = \partial\omega/\partial P = \alpha(\partial\omega/\partial T) f_2(\kappa,\rho c_p)$. ψ_{ns} is determined by the laser absorption coefficient, the temperature coefficient of the Raman shift, the volumetric heat capacity (ρc_p), and the in-plane thermal conductivity of the sample. However, the thermal diffusion length from the heating region in this state is much smaller than the steady state. That is, the contributions of heat conduction, which is highly related to the in-plane thermal conductivity of the sample, to the two Raman shift power coefficients are different for the two cases.

Based on these two Raman shift power coefficients, a dimensionless normalized RSC is defined as $\Theta = \psi_{\mathrm{ns}}/\psi_{\mathrm{CW}} = f_3(\kappa,\rho c_{\mathrm{p}})$. Although ψ_{CW} and ψ_{ns} are all influenced by the laser absorption coefficient and the temperature coefficient of the Raman shift, the effects of these two parameters are completely ruled out in this normalized RSC. The laser power used in the experiments is very low, so that the temperature rise of the sample is moderate. In our work, the volumetric heat capacity of the sample has negligible size effect and shares the same value of the bulk counterpart. Then, Θ is only related to the unknown in-plane thermal conductivity of the sample. Due to the different contributions of heat conduction under the two energy transport states, this normalized RSC could be used to obtain the in-plane thermal conductivity of samples of different thicknesses. A 3D heat conduction model is used to simulate the temperature rise under the two energy transport states. Then, a relationship between the temperature rise ratio of the two energy transport states and the in-plane thermal conductivity of the sample could be built. The in-plane thermal conductivity of the samples with different thicknesses could be finally determined based on the measured Θ.

For the steady-state heating, the energy transport in the sample is governed by the differential equation[21,22] as shown below:

$$\kappa\nabla^2 T_{\mathrm{CW}} + \dot{q} = 0 \tag{1}$$

where T_{CW} (K) is the temperature rise in steady-state heating, r is the radial position from the center of the hole, κ (W m^{-1} K^{-1}) is the in-plane thermal conductivity of the sample, and $\dot{q}$ is volumetric Gaussian beam heating and is given as

$$\dot{q}(r,z) = \frac{I_0}{\tau_{\mathrm{L}}}\exp\left(-\frac{r^2}{{r_0}^2}\right)\exp\left(-\frac{z}{\tau_{\mathrm{L}}}\right) \tag{2}$$

where $I_0 = P/\pi {r_0}^2$ is the laser power per unit area at the center of the laser spot, r_0 (μm) is the radius of the ns laser spot, τ_{L} is the laser absorption depth and could be obtained based on the equation $\tau_{\mathrm{L}} = \lambda/(4\pi k_{\mathrm{L}})$,[29] where λ (532 nm) is the laser wavelength and k_{L} the extinction coefficient of the sample. We have $\tau_{\mathrm{L}}(\mathrm{MoS_2})$ = 36.5 nm and $\tau_{\mathrm{L}}(\mathrm{MoSe_2})$ = 20.6 nm.[30,31] Note that although we used this parameter for data processing in our work, any error carried in it will have negligible effect on the finally determined κ.

For transient-state heating, the width of the ns laser pulse is 76 ns, and the interval between two pulses is 10 μs. When the laser irradiates the sample, electrons will be excited to the conduction band with holes left in the valence band. Then hot carriers (hot electrons and holes) are formed due to the higher energies compared to the Fermi energy. The life time of these hot carriers is about nanoseconds or shorter, which is much shorter than the laser pulse width. If the hot carrier life time is longer than or comparable to the laser pulse width, the effect of the hot carrier should be considered. The equation below can be used to determine the carrier concentration $\Delta N(r,t)$:[32]

$$\frac{\partial \Delta N}{\partial t} = D\nabla^2\Delta N - \frac{\Delta N}{\tau} + \frac{\partial n_0}{\partial T}\frac{\partial T}{\tau} + \Phi\beta \tag{3}$$

where D, τ, and Φ are the carrier diffusion coefficient, the electron–hole recombination time and the incident photon flux of the laser source. β and n_0 are the optical laser absorption coefficients of the material and the equilibrium free-carrier density at temperature T. This also indicates that it is very important to select an appropriate laser pulse width in the experiment. In addition to the hot carrier life time, the time needed to reach a thermal equilibrium for the material should also be considered. This time can be estimated as $t \sim d^2/\alpha$, where d and α are the diameter of the laser spot and the thermal diffusivity of the material. The laser pulse width should be comparable to or shorter than this time. For materials with a very small α, this time will be very long, and a microsecond pulsed laser may also be useful. While for materials with a very large α, this time will be very short, and a picosecond pulsed laser may be needed.

For pulsed laser heating, the effective thermal diffusion length (L_{d}) could be estimated as $L_{\mathrm{d}} = 2\sqrt{t\cdot\kappa/\rho c_{\mathrm{p}}}$,[33] where ρc_{p} (J m^{-3} K^{-1}) is the volumetric heat capacity of the sample, t (s) is laser pulse width. The diffusion length values of $\mathrm{MoS_2}$ and $\mathrm{MoSe_2}$ are about 4 and 3 μm, respectively. Note that this length is much longer than the sample thickness (around 100 nm or less). Thus, it is physically reasonable to assume that the sample has a uniform temperature distribution in the thickness direction and this has been observed in our 3D modeling. The size of the suspended area is 22 μm × 22 μm. As a result, the thermal diffusion area under this state is much smaller than the sample size. A characteristic time (t_{c}) is used to define the time needed for the temperature to cool down to the ambient temperature after nanosecond pulse heating. This time is estimated as $t_{\mathrm{c}} = 0.2026\rho c_{\mathrm{p}}L^2/\kappa$, where L (m) is the distance between the center of the suspended sample and the boundary of the suspended sample, which is 11 μm in our experiments. Due to the smaller thermal conductivity of $\mathrm{MoSe_2}$, its corresponding characteristic time is longer, which is about 4 μs. That is, the time interval between two pulses (10 μs) is long enough for the sample to cool down to the ambient temperature for $\mathrm{MoS_2}$ and $\mathrm{MoSe_2}$ after a ns pulse heating. Therefore, it is confirmed that the ns pulses do not have interference with each other and no steady-state heat accumulation exists in the ns laser heating case. The Fourier equation governing the nanosecond laser heating pulse can be written as[34]

$$\kappa\nabla^2 T_{\mathrm{ns}} + I/\tau_{\mathrm{L}} = \rho c_{\mathrm{p}}\frac{\partial T_{\mathrm{ns}}}{\partial t} \tag{4}$$

where T_{ns} is the temperature rise in the transient state. The laser intensity I (W m^{-3}) is expressed by

$$I(r,z,t) = I_0\exp\left(-\frac{r^2}{{r_0}^2}\right)\exp\left[-4\ln(2)\frac{t^2}{{t_0}^2}\right]\exp\left(-\frac{z}{\tau_{\mathrm{L}}}\right) \tag{5}$$

where I_0 (W m^{-2}) is the peak laser intensity, and t_0 (76 ns) is the pulse width of the ns laser.

Based on eqn (1) and (4), the measured temperature rises of the sample under the two energy transport states are determined by the in-plane thermal conductivity, the laser absorption coefficient and the volumetric heat capacity. By solving eqn (1) and (4), the ratio of the temperature rises of the sample under the two heating states could be obtained. In our experiments, the ratio is equal to the normalized RSC. As the temperature rise caused by laser heating is moderate, ρc_p could be assumed constant. As a result, the ratio could be used to determine the in-plane thermal conductivity of the sample based on the different contributions of heat conduction under the two energy transport states. Note the experimental data (RSC) basically are based on Raman intensity-weighted temperature rises in both time and space. All these are considered in our data processing and detailed later.

A schematic diagram of the Raman system setup for the experiments is shown in Fig. 2 (see Methods for more details). Fig. 2(c) shows the Raman spectra of two vibrational modes of MoS_2 ($E_{2g}{}^1$ and A_{1g}) and one vibration mode of $MoSe_2$ (A_{1g}) excited by the 532 nm laser. The $E_{2g}{}^1$ mode of MoS_2 is associated with the in-plane opposite vibration of two sulfur atoms with respect to the molybdenum atom, while the A_{1g} modes of the two materials are related to the out-of-plane vibration of only sulfur or selenium atoms in opposite directions.[24,35]

Sample preparation and characterization

Four layered MoS_2 samples and four layered $MoSe_2$ samples are prepared by the mechanical exfoliation method from bulk MoS_2 and bulk $MoSe_2$ crystals, respectively (see Methods for more details). Compared with samples prepared by chemical vapor deposition and liquid exfoliation, samples with pristine, clean, and high-quality structures could be obtained by using the mechanical exfoliation method.[36] Adhesive Scotch tape and gel films (Gel-Film, PF-20/1.5-X4, Gel-Pak) are used to transfer the MoS_2 or $MoSe_2$ nanosheet to a clean silicon substrate with a hole beneath.[37] The hole is fabricated using the focused ion beam (FIB) technique. The size of the hole is 22 μm × 22 μm, and the depth of the hole is 3 μm. Fig. 3 shows the process of sample preparation.

Fig. 4(a)–(h) show the AFM images of the four MoS_2 samples and four $MoSe_2$ samples. To avoid sample damage, the supported areas of these samples are used to measure the thickness of the samples. In these images, the red dashed lines indicate the thickness profiles shown below. The thicknesses of MoS_2 samples are 45, 81, 102, and 115 nm, respectively. The thicknesses of $MoSe_2$ samples are 45, 62, 95, and 140 nm, respectively. The biggest thickness variation (Δl_{max}) along the line of the sample surface is used to evaluate the surface roughness. As shown in the figures, compared with the thickness of the samples, the values of Δl_{max} for these samples are relatively small. Δl_{max} increases with an increase in thickness. In addition to surface roughness, wrinkles on these samples can also result in thickness variation. For the 62 nm $MoSe_2$, Δl_{max} is a bit larger, which is possibly induced by the relatively larger space between the sample and the substrate in some locations. The root-mean-square roughness (R_q) is also used to reflect the roughness of the samples. For instance, R_q of the four MoS_2 samples are 1.73, 1.95, 2.61, and 3.05 nm, respectively. It can be seen that R_q increases a little with an increase in thickness.

In this work, the nanosecond ET-Raman technique is used to measure these nm-thick MoS_2 and $MoSe_2$. For a μm-thick sample, this technique is still applicable. However, the temperature distribution in the thickness direction will not be uniform, which means that the thermal transport in this direction cannot be neglected. If the thermal conductivity of the material is isotropic, this technique can be used directly. Technique modification is needed if the thermal conductivity of the material is anisotropic. In this case, one more transient state with a different laser heating size is needed. These two

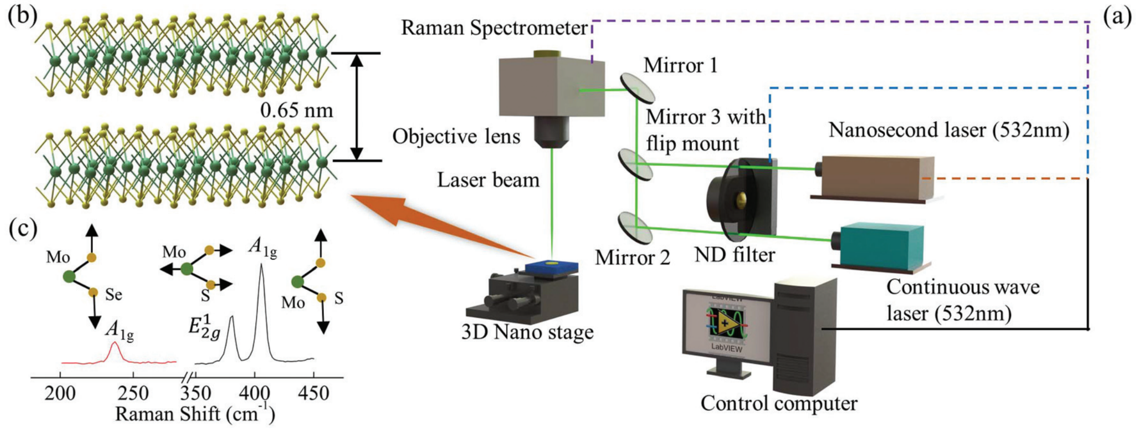

Fig. 2 Schematic diagram of the ns ET-Raman system. (a) A suspended 2D atomic-layer sample (MoS_2 or $MoSe_2$) is irradiated by CW and ns lasers. A LabVIEW-based software program is used to control the Raman spectrometer and the ND filter. (b) The atomic structure of MoS_2 or $MoSe_2$. The green balls are the Mo atoms, and the yellow balls are sulfur or selenium atoms. The distance between two adjacent layers is around 0.65 nm. (c) Raman spectra of MoS_2 and $MoSe_2$ excited by the laser could be used to determine the temperature rise of the sample. $E_{2g}{}^1$ (~383 cm^{-1}) and A_{1g} (~408 cm^{-1}) modes of MoS_2, and the A_{1g} (~240 cm^{-1}) mode of $MoSe_2$ are obtained in the experiments. The A_{1g} modes for both MoS_2 and $MoSe_2$ are used to explore the temperature rise of the samples.

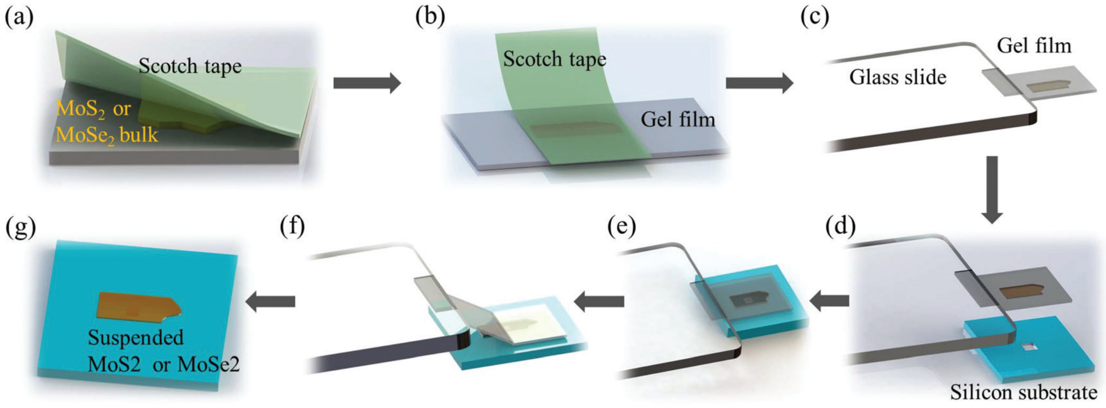

Fig. 3 Schematic diagram of the sample preparation process for the Raman experiments. (a) MoS_2 or $MoSe_2$ are peeled off from the bulk materials using the mechanical exfoliation method. (b) The exfoliated material is then transferred from the Scotch tape to a gel film. (c) The gel film is attached to the edge of the glass slide. (d) Alignment of the gel film with the hole in the silicon substrate by using two 3D nano-stages. (e) The gel film is then moved down to touch the silicon substrate. (f) The gel film is moved up slowly to realize the transfer of the sample to the silicon substrate. (g) The obtained suspended MoS_2 or $MoSe_2$ on the silicon substrate.

transient states can be constructed by using two objectives of different magnifications, such as 20× and 100×. Due to the difference between the two laser heating areas, the contributions of the thermal conductivity in the thickness direction are different in these two states. Combining these two transient states with the steady state, the thermal conductivity of the material in the two directions could be determined. At present, we are using this method to measure the anisotropic thermal conductivity of bulk $MoSe_2$. Results will be reported in our near-future publications.

Thermal response of the sample under CW and ns laser heating

In the Raman experiments, room temperature Raman spectra are collected automatically under different laser powers for all the eight samples to obtain the Raman shift power coefficient. Both the CW and ns laser power are adjusted based on the material and thickness of the sample. For the 45 nm thick MoS_2 sample, the CW laser power is varied from 0.31 mW to 1.82 mW under the 20× objective lens, and the ns laser power is from 0.023 mW to 0.071 mW under the 20× objective lens. The laser powers of all the eight samples are listed in Table 1. Note that the laser power here refers to the average power of the laser irradiating the sample surface. The laser power should be maintained as low as possible to avoid sample damage[38] and to stay within the linear dependence range of the Raman shift. The diameters of the two laser spots on different samples are also measured. First, the optical images of the laser spots are captured with a CCD (charge-coupled-device) camera (Olympus DP-26, Olympus Optical Co., Ltd). Then these images are analyzed based on a Gaussian fitting method to calculate the diameters of the laser spots. The obtained values of the diameters (at e^{-1} of the center intensity) of the laser spots on the eight samples are also listed in Table 1. It can be seen that there are some differences among the laser spots on different samples and between the two lasers on the same sample. These differences are induced by the difference between the two lasers, the surface quality of the suspended samples, and the slight variation of the focusing level during the experiment. As the nanosecond ET-Raman technique is based on the assumption of diffusive and local-equilibrium thermal transport, it is necessary to compare the laser spot size with the phonon mean free path (MFP) of the sample. For the high end, the phonon MFP of graphene is about 600 nm [39] and the modal MFP of some flexural acoustic (ZA) modes can be several microns.[40] This is much longer than that of other materials. The phonon mean free path of MoS_2 or $MoSe_2$ is much shorter. The diameter of the laser spot sizes in our work is about 2.4 μm or larger. That is, the laser spot sizes of the two transport states are much longer than the phonon mean free path of MoS_2 or $MoSe_2$. Thus, we can take the thermal transport as diffusive and local-equilibrium. At present we are using the nanosecond ET-Raman to measure the anisotropic thermal conductivity of graphene paper. Due to the long phonon mean free path of graphene, we already found that when we used a 100× objective lens, non-diffusive and local non-equilibrium transport was detected. This is because the diameter of the laser spot under a 100× objective lens is about 600 nm, comparable to the phonon mean free path of graphene. Results will be reported in our near-future publications.

The 45 nm thick MoS_2 and 45 nm thick $MoSe_2$ are used to explain the results. Fig. 5(a) and (b) show the 3D contour maps of the MoS_2 Raman peaks at 380 cm^{-1} and 405 cm^{-1} under different laser powers of the two lasers to give an overall picture of how the Raman intensity of the two peaks varies with the laser power. That is, the Raman intensity increases linearly with the increase of laser power. As shown in Fig. 5(a), the linearity at some data points is not very good, which may be induced by the Gaussian fitting errors of the Raman spectra. This could also be caused by the laser heating effect. With the laser irradiating the sample, the local temperature

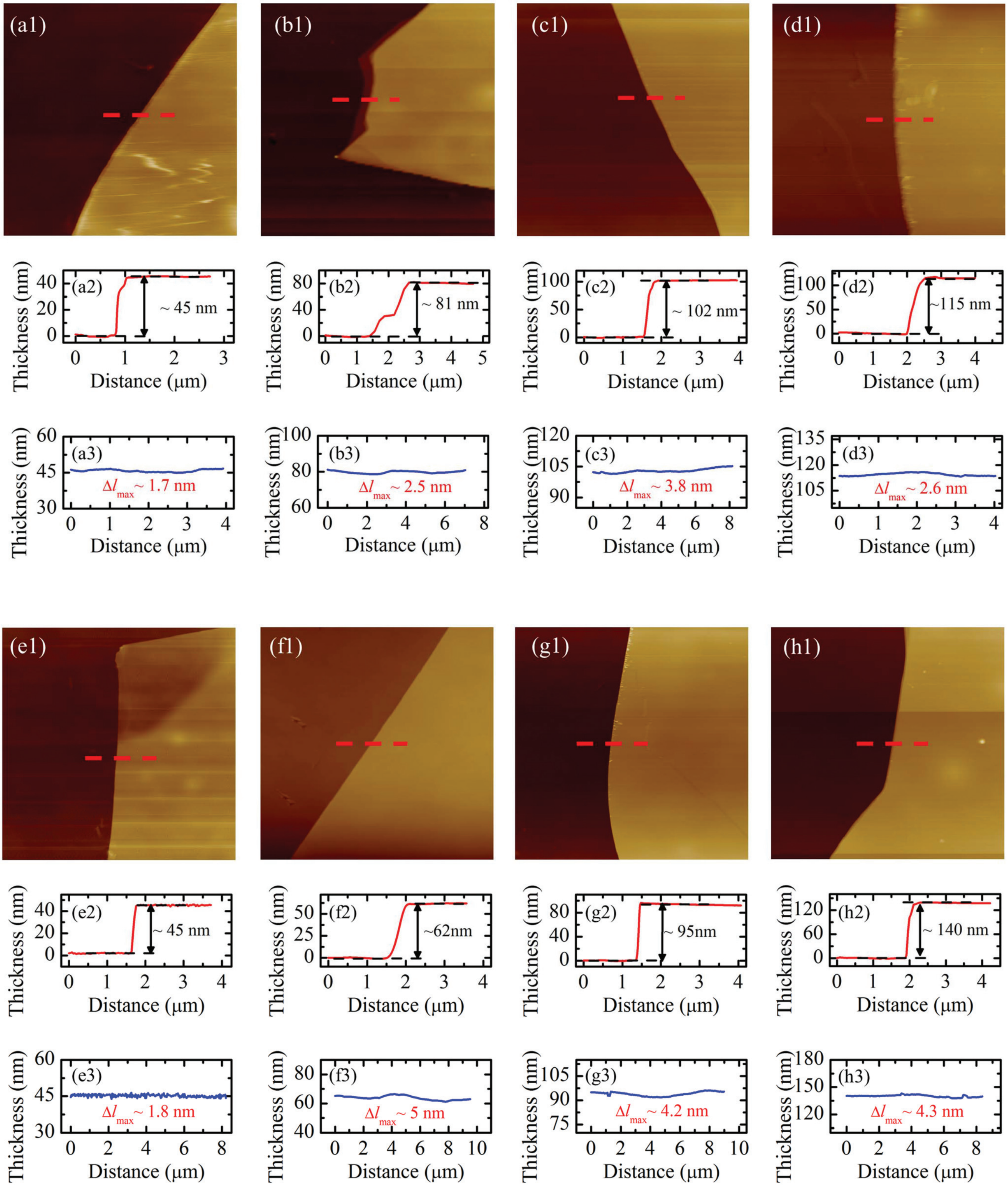

Fig. 4 (a–d) AFM measurement results of four suspended MoS_2 samples. (e–h) AFM measurement results of four suspended $MoSe_2$ samples. (a1–h1) are the AFM images. (a2–h2) are the thickness profiles to show the thickness of the sample corresponding to the red dashed line in the AFM images. (a3–h3) are the thickness profiles to indicate the roughness of the eight samples.

Table 1 Summary of the CW and ns laser power ranges for the eight samples and the corresponding laser spot diameters under the two lasers

Sample thickness (nm)	Sample materials	CW laser power range under the 20× objective lens (mW)	ns laser power range under the 20× objective lens (mW)	CW laser spot diameter (μm)	ns laser spot diameter (μm)
45	MoS_2	0.31–1.82	0.023–0.071	3.294	2.509
81	MoS_2	0.58–3.41	0.019–0.112	3.232	2.423
102	MoS_2	0.67–3.29	0.046–0.178	3.251	2.492
115	MoS_2	0.67–3.93	0.046–0.178	2.846	2.460
45	$MoSe_2$	0.34–1.97	0.046–0.178	3.089	2.471
62	$MoSe_2$	0.40–1.95	0.046–0.178	2.843	2.562
95	$MoSe_2$	0.44–2.12	0.042–0.200	3.293	2.397
140	$MoSe_2$	0.36–1.76	0.042–0.200	3.011	2.400

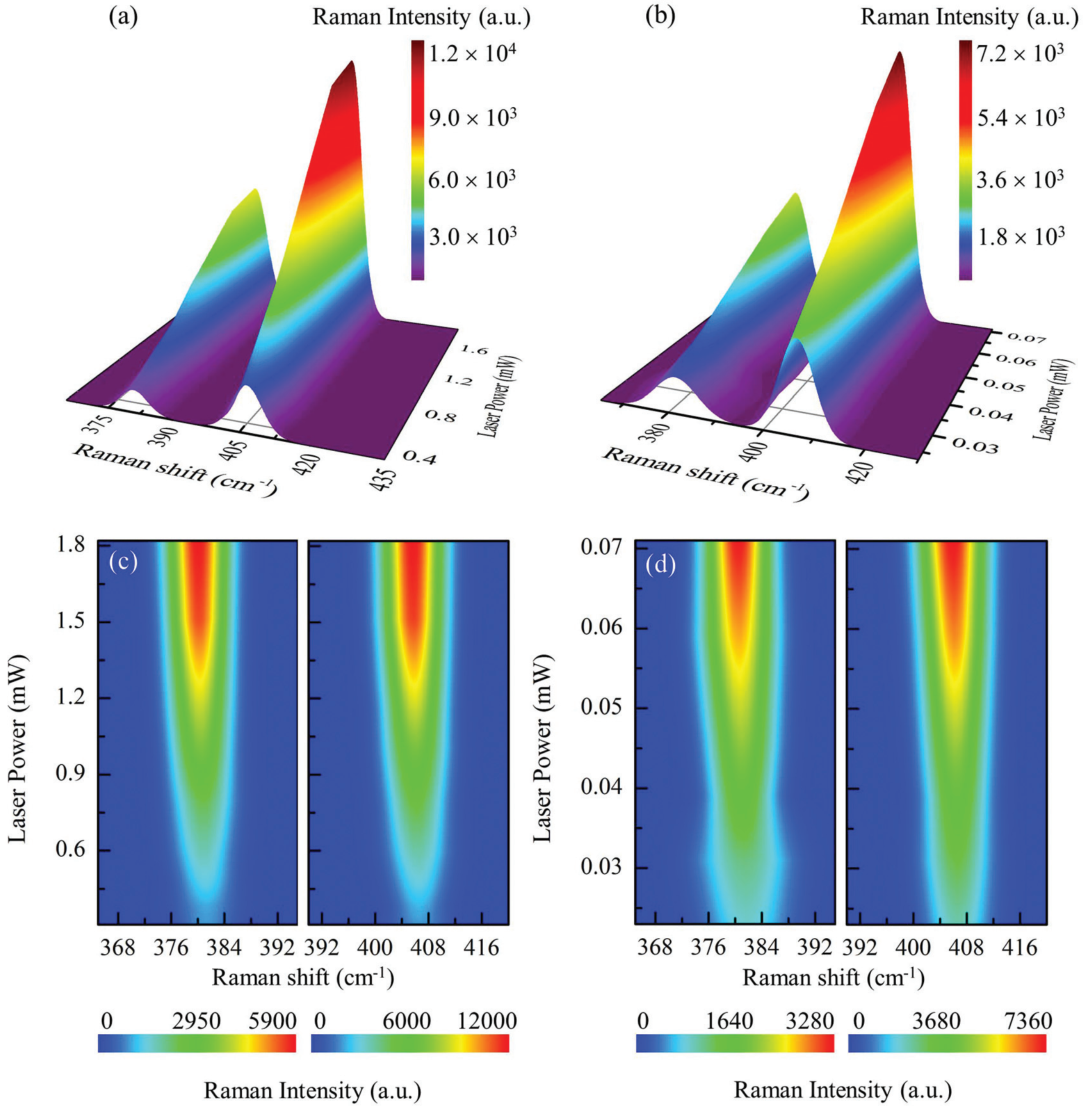

Fig. 5 Contour maps of MoS_2 Raman peaks. The 45 nm-thick sample is used to illustrate the ns ET-Raman experimental results. Both a CW laser and a ns laser are used to generate different energy transport states. (a) and (b) are the 3D contour maps to demonstrate the variation of Raman intensity against the laser power of the CW laser and ns laser, respectively. (c) and (d) are the 2D contour maps to demonstrate the variation of Raman shift against the laser power of the CW laser and ns laser, respectively.

will increase, and the detected Raman intensity will decrease. Fig. 5(c) and (d) are also the contour maps of the two Raman peaks to indicate that the two Raman peaks will be redshifted with the increase of laser power. Five representative room temperature Raman spectra of MoS_2 under CW laser and ns laser are shown in Fig. 6(a) and (b), respectively. It can also be

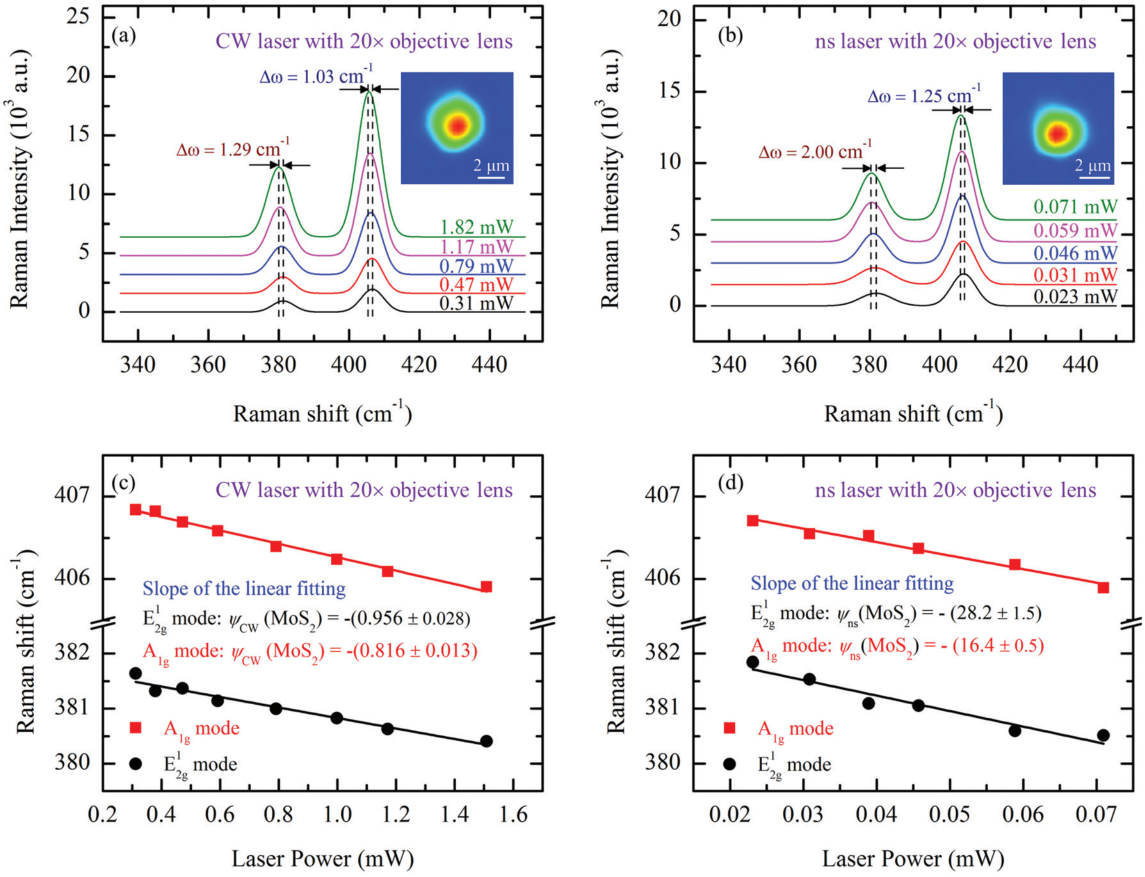

Fig. 6 Raman spectra of 45 nm-thick suspended MoS_2. (a) Five representative Raman spectra of MoS_2 with increased laser power under CW laser with the 20× objective lens at room temperature. The variations of Raman shifts for the two modes of MoS_2 are 1.29 cm^{-1} and 1.03 cm^{-1}, respectively. (b) Five representative Raman spectra of MoS_2 with increased laser power under a ns laser with the 20× objective lens at room temperature. The variations of Raman shifts for the two modes of MoS_2 are 2.00 cm^{-1} and 1.25 cm^{-1}, respectively. The spots of the two lasers are also shown in (a) and (b). For the two lasers, the Raman shifts of the two modes as a function of laser power are shown in (c) and (d), respectively. The solid lines in the two figures are the fitting results to obtain the linear power coefficient.

seen that both the Raman peaks of MoS_2 are red-shifted with the increase of laser power. This indicates the local temperature of the sample is increasing with the increase of laser power. We show the power-dependent peak positions in the linear, low-power range by using $\Delta\omega = \omega(P_2) - \omega(P_1) = \psi(P_2 - P_1) = \psi\Delta P$. As shown in Fig. 6(c) and (d), the positions of the two peaks of MoS_2 have a good linear relationship with the laser power. In this work, the A_{1g} mode of MoS_2 is chosen to deduce RSC since the $E_{2g}{}^1$ mode is prone to strain while A_{1g} is not.[41] It can be seen in Fig. 6(c) and (d) that the linear fitting results RSC of the A_{1g} mode under the CW laser is $-(0.816 \pm 0.013)$ cm^{-1} mW^{-1}, and under the ns laser it is $-(16.4 \pm 0.5)$ cm^{-1} mW^{-1}. When the average energy inputs of the two lasers are the same, the pulse power of the ns laser will be very high, and the thermal diffusion length under the ns laser is also much smaller than that under the CW laser. As a result, the temperature rise of the sample irradiated by the ns laser will be much higher than that for the CW laser, and the RSC values under the ns laser will also be much larger than that under the CW laser.

Fig. 7(a) and (b) show the 3D contour maps of the $MoSe_2$ Raman peak at ~240 cm^{-1} under different laser powers of the two different lasers. The Raman intensity of this peak is also linearly related to the laser power. Fig. 7(c) and (d) are contour maps of this Raman peak to show that the peak will also be redshifted with the increase of laser power. Five representative room temperature Raman spectra under the two lasers are also shown in Fig. 8(a) and (b). A redshift of the Raman peak could also be seen. It can be seen in Fig. 8(c) and (d) that the shift of the peak of $MoSe_2$ is also linearly related to the laser power. The linear fitting results RSC of the A_{1g} mode under CW laser is $-(0.974 \pm 0.017)$ cm^{-1} mW^{-1}, and under ns laser it is $-(7.48 \pm 0.18)$ cm^{-1} mW^{-1}. The RSC values for all the eight samples are listed in Table 2. The RSC values roughly decrease with the increase of thickness of the samples for both CW and ns laser heating, which indicates the increase of the in-plane thermal conductance of the sample *versus* the sample thickness. As the thicknesses of all the samples are larger than the laser absorption depth of the corresponding materials, the absorbed energy will be nearly the same for samples with different thick-

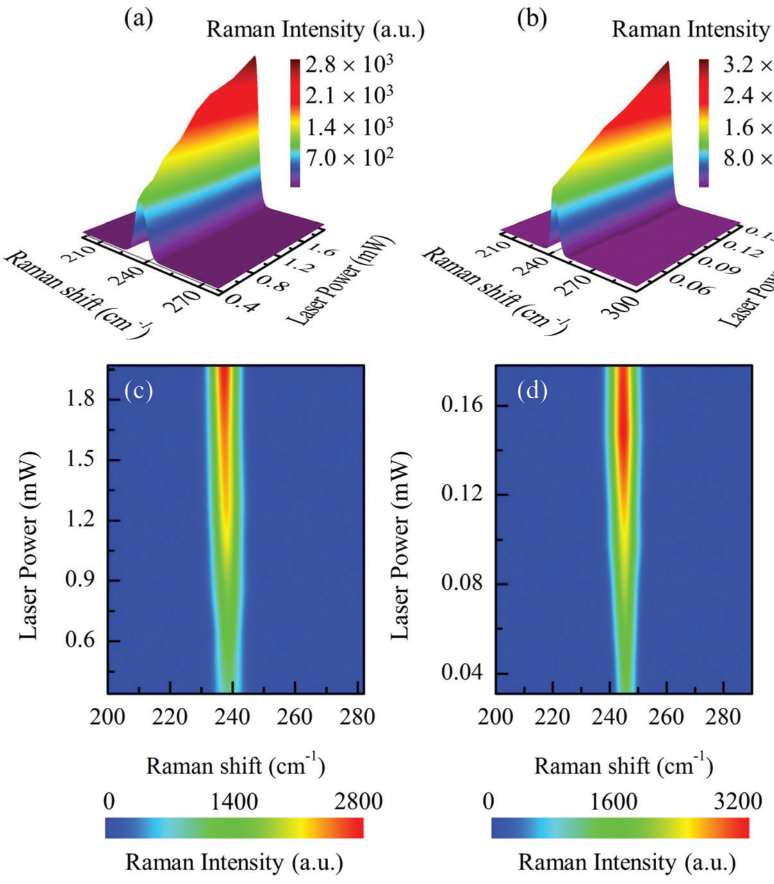

Fig. 7 Contour maps of the $MoSe_2$ Raman peak. The 45 nm-thick sample is used to illustrate the ns ET-Raman experimental results. (a) and (b) are the 3D contour maps to demonstrate the variation of Raman intensity against the laser power of the CW laser and ns laser, respectively. (c) and (d) are the 2D contour maps to demonstrate the variation of Raman shift against the laser power of CW laser and ns laser, respectively.

nesses. However, the temperature rise is decreasing, which means that the temperature rise is smaller for thicker samples. For thicker samples, the in-plane thermal conductance is larger due to the larger heat conduction cross-section. As a result, the temperature rise will be smaller for thicker samples.

Determination of thermal conductivity

By combining these two RSC values of CW and ns lasers, a normalized RSC (Θ) is obtained, and the values of the eight samples are summarized in Table 2. These values listed in Table 2 indicate that Θ increases with the increase of thickness of MoS_2 and $MoSe_2$. Then a 3D numerical modeling based on the finite volume method is conducted to calculate the temperature rise under the two energy transport states to determine the in-plane thermal conductivity of MoS_2 and $MoSe_2$ with different thicknesses. Fig. 9(a) and (b) show the 3D numerical modeling process under the steady state and the transient state, respectively. The laser power used in the simulation is also very low (0.05 mW) to ensure a small temperature rise. The corresponding laser spot size measured in the experiment is also used in the simulation to guarantee the simulation accuracy. A Raman intensity weighted average temperature over space ($\bar{T}_{CW}/_{Theoretical}$) under the steady state and a Raman intensity weighted average temperature over space and time ($\bar{T}_{ns}/_{Theoretical}$) under the transient state are obtained. This simulation process is performed for different κ values. Then the ratios of these two values: $\Theta/_{Theoretical} = ((\bar{T}_{ns}/_{Theoretical} - 22)/(\bar{T}_{CW}/_{Theoretical} - 22))$ under different trial κ values are used to determine the theoretical curve of Θ against κ. Here “22” is the initial temperature of the sample.

Fig. 10(a) and (b) show the temperature rise of 45 nm-thick MoS_2 and 45 nm-thick $MoSe_2$ under the two energy transport states in our modeling. Fig. 10(c) and (d) show the theoretical Θ curves of these two samples. The values obtained in the experiments could be interpolated to determine κ of the samples. As shown in these two figures, the κ values of 45 nm-thick MoS_2 and 45 nm-thick $MoSe_2$ are 40.0 ± 2.2, and 11.1 ± 0.4 W m^{-1} K^{-1}, respectively. Also, the final results and the uncertainty for the other six samples are summarized in Table 3. In this work, ρc_p and κ are assumed to be constant. Here the 45 nm-thick MoS_2 sample is used to justify this assumption. The Raman shift change ($\Delta\omega$) of this sample under laser irradiation is 0.98 cm^{-1} in the CW case. The Raman temperature coefficient (η) is around 0.0123 cm^{-1} K^{-1}.[28] Then the temperature rise of the sample under the laser spot can be calculated as $\bar{T}_{Ra} = \Delta\omega/\eta = 80$ K. The thermophysical properties

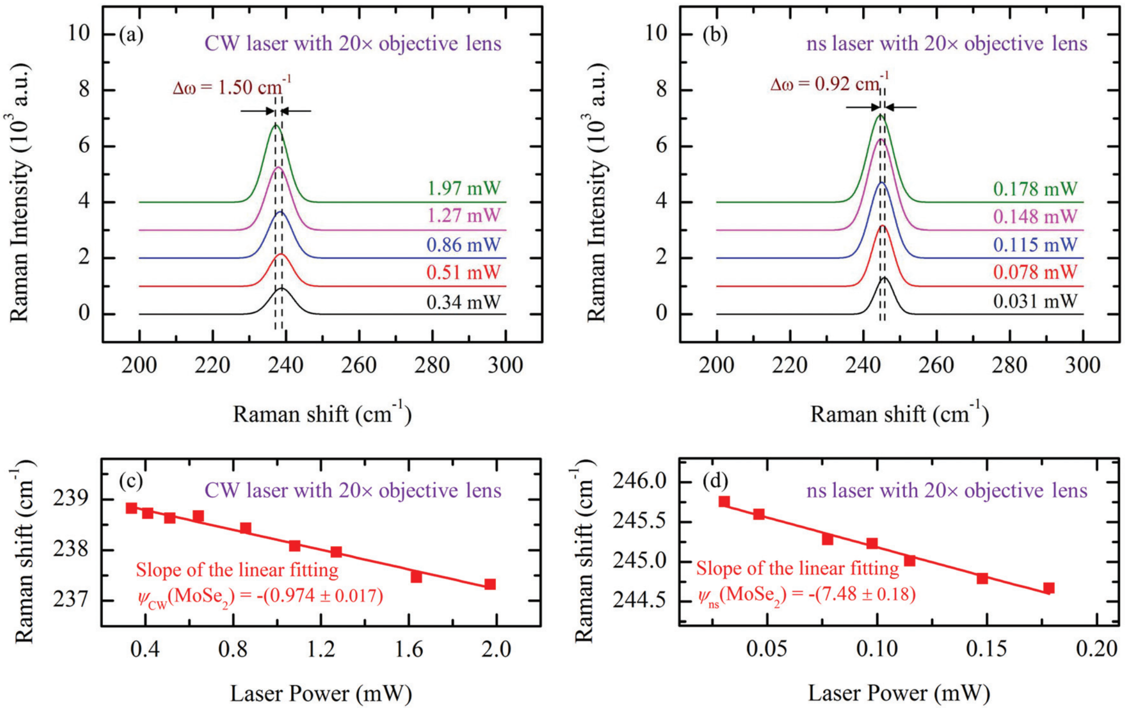

Fig. 8 Raman spectra of 45 nm-thick suspended $MoSe_2$. (a) Five representative Raman spectra of MoS_2 with increased laser power under a CW laser with the 20× objective lens at room temperature. The variation of the Raman shift of $MoSe_2$ is 1.50 cm^{-1}. (b) Five representative Raman spectra of $MoSe_2$ with increased laser power under a ns laser with the 20× objective lens at room temperature. The variation of Raman shift of $MoSe_2$ is 0.92 cm^{-1}. For the two lasers, the Raman shifts as a function of laser power are shown in figure (c) and (d), respectively. The solid lines in the two figures are the fitting results to obtain the linear power coefficient.

Table 2 Summary of the A_{1g} mode RSC values under the two lasers for the eight samples

Sample thickness (nm)	Sample materials	A_{1g} mode RSC under the CW laser (cm^{-1} mW^{-1})	A_{1g} mode RSC under the ns laser (cm^{-1} mW^{-1})	Normalized RSC
45	MoS_2	−(0.816 ± 0.013)	−(16.4 ± 0.5)	20.09 ± 0.69
81	MoS_2	−(0.322 ± 0.007)	−(8.36 ± 0.19)	25.98 ± 0.82
102	MoS_2	−(0.299 ± 0.004)	−(8.12 ± 0.15)	27.17 ± 0.62
115	MoS_2	−(0.268 ± 0.005)	−(7.44 ± 0.10)	27.73 ± 0.64
45	$MoSe_2$	−(0.974 ± 0.017)	−(7.48 ± 0.18)	7.68 ± 0.23
62	$MoSe_2$	−(0.876 ± 0.014)	−(7.75 ± 0.18)	8.84 ± 0.25
95	$MoSe_2$	−(0.553 ± 0.009)	−(6.20 ± 0.13)	11.22 ± 0.30
140	$MoSe_2$	−(0.529 ± 0.011)	−(6.95 ± 0.19)	13.15 ± 0.45

of the sample are determined by the average temperature rise of the entire sample. This temperature rise can be calculated as $\overline{T}_s = \int 2\pi r T \mathrm{d}r/(\pi r_0{}^2)$, where r is the distance to the sample's middle point. Using these two values and the theoretical Raman intensity weighted temperature $\bar{T}_{\mathrm{CW}}/_{\mathrm{Theoretical}}$ that is shown in Fig. 9(a), the average temperature rise of the sample in all domains is determined based on $\bar{T}_{\mathrm{sa}} = \bar{T}_{\mathrm{s}}\cdot\bar{T}_{\mathrm{Ra}}/(\bar{T}_{\mathrm{CW}}/_{\mathrm{Theoretical}} - 22)$. The obtained $\bar{T}_{\mathrm{sa}}$ is about 25 K, which is small enough to assume that κ is a constant for the experiment. Also, as shown in Fig. 6(c) and (d), the Raman shift change of the ns case is close to the CW case. Therefore, the average temperature rise for the ns case is also close to the CW case. As a result, ρc_{p} can also be assumed constant during the thermal characterization.

As shown in Table 3, the measured in-plane thermal conductivity of suspended MoS_2 films and suspended $MoSe_2$ films increases with the increase of film thickness. For MoS_2, when the thickness increases from 45 nm to 115 nm, the corresponding thermal conductivity increases from 40.0 ± 2.2 to 74.3 ± 3.2 W m^{-1} K^{-1}. The thermal conductivity of 115 nm-thickness MoS_2 is about 86% higher than that of the 45 nm-thickness MoS_2. For $MoSe_2$, when the thickness increases from 45 nm to 140 nm, the corresponding thermal conductivity increases from 11.1 ± 0.4 to 20.3 ± 0.9 W m^{-1} K^{-1}. The thermal conductivity of 140 nm-thickness $MoSe_2$ is about 83% higher than that of the 45 nm-thickness $MoSe_2$. To explore the relationship between the in-plane thermal conductivity and the thickness of these two materials, the thermal

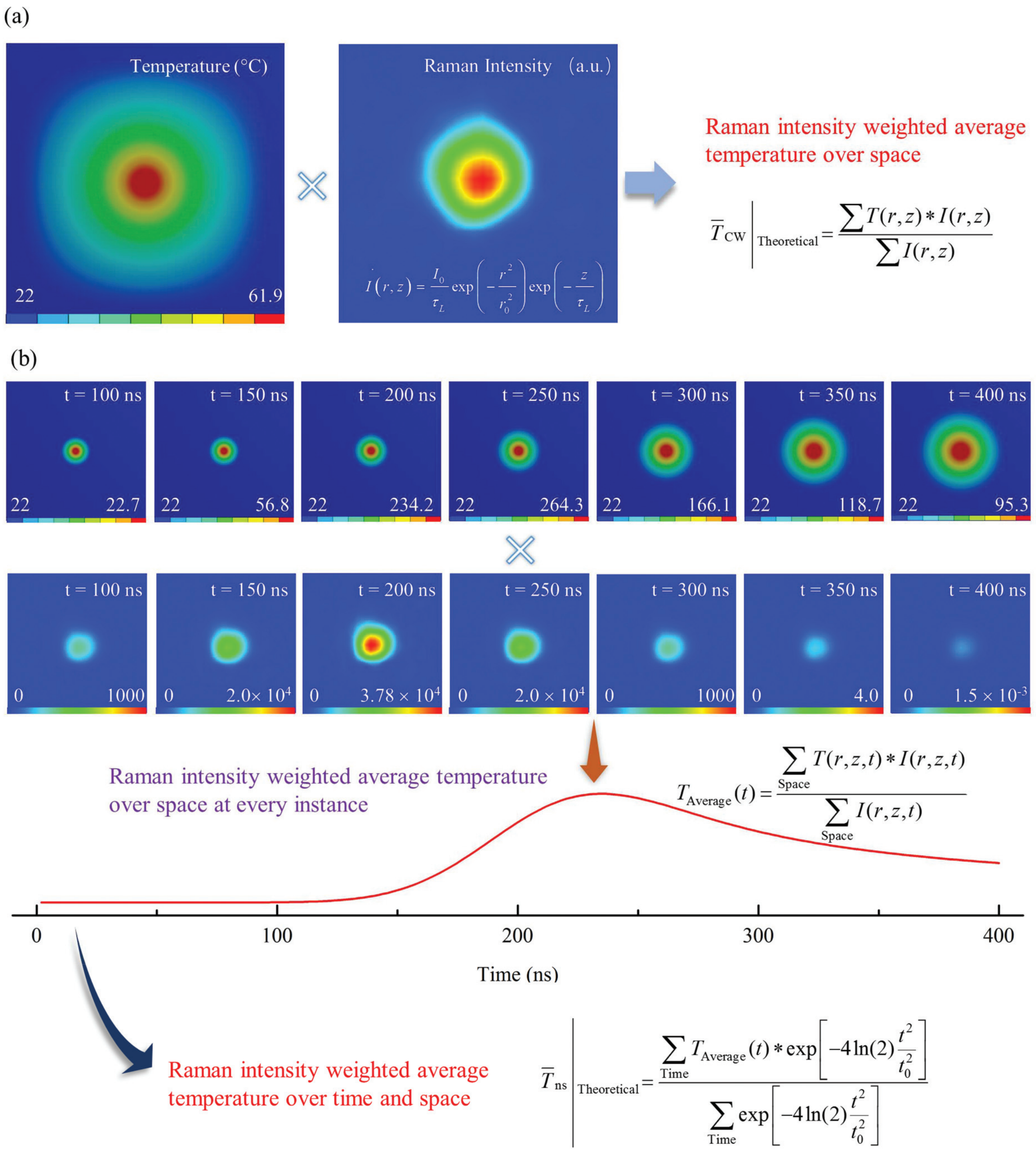

Fig. 9 3D numerical modeling process of ns ET-Raman. (a) Simulation of the heat conduction under a CW laser; a Raman intensity weighted average temperature over space domain is obtained based on the temperature and Raman intensity distribution in the space domain. (b) Simulation of the heat conduction under ns laser; a Raman intensity weighted average temperature in the time and space domains is obtained based on the temperature and Raman intensity distribution in the time and space domains.

conductivities of different thicknesses obtained in our work and previous studies are summarized in Fig. 11(a) and (b).[24,25,28,41–49]

As shown in these two figures, different values of thermal conductivity for samples with the same number of layers are observed. The difference can be attributed to three factors. First, the quality of the prepared samples and the measurement methods are different.[41] For atomic-layer materials, the influence of the surface roughness and the wrinkles on the thermal conductivity could not be neglected. As the disadvantages of different measurement methods could induce different errors, the measured thermal conductivity could also be different. Second, a discrepancy exists among the obtained temperature coefficients of the samples in the reported works using temperature-dependent Raman spectroscopy. This discrepancy is possibly related to the different strain effects on

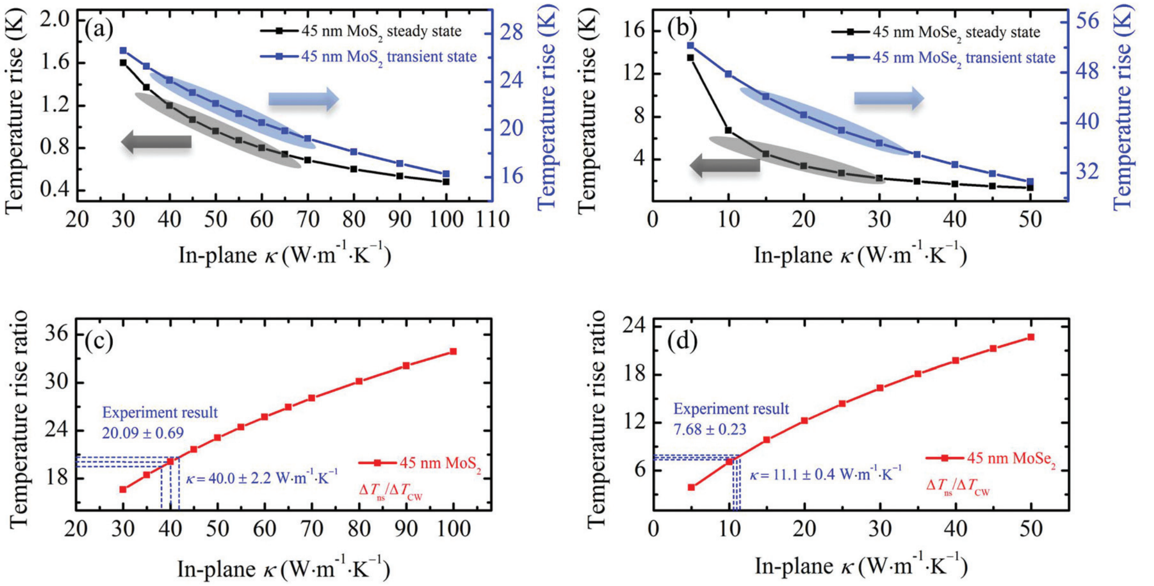

Fig. 10 3D numerical modeling results for the 45 nm thick MoS$_2$ sample and the 45 nm thick MoSe$_2$ sample. (a) and (b) show the average temperature rises of MoS$_2$ and MoSe$_2$ under the two energy transport states with the increase of in-plane thermal conductivity, respectively. (c) and (d) show the relationship between the ratio of temperature rises under the two energy transport states and the in-plane thermal conductivity of the samples. The in-plane thermal conductivity of the samples is obtained by interpolating the modeling results based on the experimental data.

Table 3 Summary of the in-plane thermal conductivity (κ) determined based on the 3D numerical modeling and experiments

Sample thickness (nm)	Sample materials	κ (W m^{-1} K^{-1})	Sample thickness (nm)	Sample materials	κ (W m^{-1} K^{-1})
45	MoS$_2$	40.0 ± 2.2	45	MoSe$_2$	11.1 ± 0.4
81	MoS$_2$	57.7 ± 3.2	62	MoSe$_2$	14.9 ± 0.5
102	MoS$_2$	65.8 ± 2.7	95	MoSe$_2$	16.0 ± 0.6
115	MoS$_2$	74.3 ± 3.2	140	MoSe$_2$	20.3 ± 0.9

samples with different sizes. Third, the laser absorption coefficient is a very important parameter in the widely used optothermal method based on Raman spectroscopy. However, the coefficient used in different papers is not the same. There can be about 57% difference among these values.[25] As a result, the measured thermal conductivity can also be varied significantly.

As shown in Fig. 11(a) and (b), when the thickness of the samples is less than 3 nm, there is a trend of decreasing in-plane thermal conductivity with the increase of thickness. This is related to the following two factors. The first one is the change in phonon dispersion.[50] For monolayer MoS$_2$ or

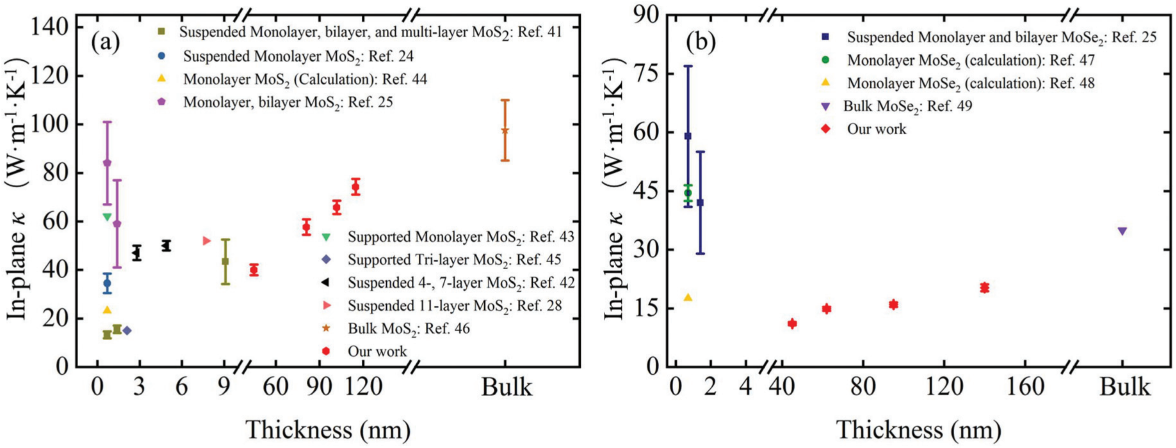

Fig. 11 (a) Summary of the in-plane thermal conductivities of the MoS$_2$ films in this study and in previous studies. (b) Summary of the in-plane thermal conductivities of the MoSe$_2$ films in this study and in previous studies.

$MoSe_2$, there are three acoustic branches, including the longitudinal acoustic (LA) branch, the transverse acoustic (TA) branch, and the ZA branch. For few-layered MoS_2 or $MoSe_2$ ($N \leq 4$), there are $3N - 3$ low-frequency optical phonon branches in addition to the three acoustic branches. A phenomenon named avoided-crossing, which reduces the average group velocity for the heat carrying phonons, could be observed among the optical phonon branches. The thermal conductivity decreases due to the lower group velocity. However, due to the low density and small velocity of the optical phonons, the effect of this factor is quite limited. The other factor is Umklapp scattering resulting from crystal anharmonicity.[25]

In monolayer MoS_2 or $MoSe_2$, Umklapp scattering is quenched and the thermal conductivity is affected mostly by the edge boundary scattering. In few-layered samples, the scattering rates of ZA phonons are significantly larger, which means that Umklapp scattering plays a much more important role in deterring the thermal conductivity of the samples. For thicker samples, the trend of increasing in-plane thermal conductivity with the increase of thickness is clearly observed for both the suspended MoS_2 films and the suspended $MoSe_2$ films. The thickness dependence of MoS_2 and $MoSe_2$ originates from significant surface scattering of long mean free path (long-MFP) phonons. Similar results have been observed in few-layered black phosphorus[23] and few-quintuple-layered Bi_2Te_3 films,[51] where surface scattering was found to heavily affect electron and phonon transport.

The surface scattering effect of phonons is analyzed below to explain the thickness-dependent thermal conductivity. By solving the phonon Boltzmann equation using the Landauer approach, the thermal conductivity could be expressed as[23,51,52]

$$\kappa = K_0 \int M_{\mathrm{ph}}(\varepsilon)\lambda_{\mathrm{ph}}(\varepsilon, T)W_{\mathrm{ph}}(\varepsilon, T)\mathrm{d}\varepsilon \tag{6}$$

where $K_0 = \pi^2 k_B T/3h$ is the quantum of thermal conductance, M_{ph} is the number of conducting modes per cross-sectional area, λ_{ph} is the phonon MFP for backscattering, which includes Umklapp phonon–phonon scattering and surface scattering. $W_{\mathrm{ph}}(\varepsilon,T) = (3\varepsilon/\pi^2 {k_B}^2 T)[\partial n_{\mathrm{BE}}(\varepsilon,T)/\partial T]$ is a normalized 'window function' with n_{BE} being the Bose–Einstein distribution and ε the phonon energy. In our work, the experiments are conducted at room temperature, and the laser heating effect is also very moderate. The phonon dispersion is also nearly the same for samples with different thicknesses. Conclusively, the effects of $M_{\mathrm{ph}}(\varepsilon)$ and $W_{\mathrm{ph}}(\varepsilon,T)$ could be neglected. Only the effect of λ_{ph} should be considered. The MFP for MoS_2 and $MoSe_2$ films is obtained by including the effect of surface scattering using the Fuchs–Sondheimer approach[51,52]

$$\lambda_{\mathrm{ph}}(E) = \lambda_{\mathrm{bulk}}\left[1 - \frac{3(1-p)}{2\delta}\int_1^{\infty}\left(\frac{1}{x^3} - \frac{1}{x^5}\right)\frac{1 - e^{-\delta x}}{1 - pe^{-\delta x}}\mathrm{d}x\right] \tag{7}$$

where $\delta = (4/3)t/\lambda_{\mathrm{bulk}}$, t is the thickness of the film and p is the specularity parameter controlling the degree of resistive scattering at the surface, with $p = 0$ and 1 corresponding to completely diffuse and specular scattering, respectively. Based on eqn (7), the MFP is longer for thicker films, which means a weaker surface scattering effect for thicker films. As a result, the corresponding in-plane thermal conductivity is also higher for thicker films.

Conclusion

A novel technique, entitled ns ET-Raman, was developed to measure the in-plane thermal conductivity (κ) of suspended 2D atomic-layer MoS_2 and $MoSe_2$ with different thicknesses. A continuous wave laser and a nanosecond pulsed laser were applied to heat and excite the Raman signal. The resulting temperature rises, which were related to κ of the sample, are measured by the power differential of the Raman shift under the two energy transport states. Due to the different thermal diffusion lengths under the two energy transport states, κ was determined by the ratio of the two Raman shift power coefficients without knowing the laser absorption and temperature coefficients of MoS_2 and $MoSe_2$. κ was observed to increase with the thickness of both MoS_2 and $MoSe_2$. For MoS_2, κ increased from 40.0 ± 2.2 to 74.3 ± 3.2 W m^{-1} K^{-1}. For $MoSe_2$, κ increased from 11.1 ± 0.4 to 20.3 ± 0.9 W m^{-1} K^{-1}. This thickness dependence was interpreted by the increased significance of surface phonon scattering in thinner samples. ns ET-Raman could also be used to determine the thermal conductivity of other 2D materials with high accuracy and confidence.

Methods

Layered MoS_2 and $MoSe_2$ sample preparation

We prepare four layered MoS_2 samples and four layered $MoSe_2$ samples by the mechanical exfoliation method from bulk MoS_2 and bulk $MoSe_2$ crystals, respectively. First, MoS_2 or $MoSe_2$ are peeled off from the corresponding bulk materials using the adhesive Scotch tape. The obtained MoS_2 or $MoSe_2$ on the tapes are then transferred to the gel films. The gel films and the silicon substrate with a hole in the middle are attached to two glass slides, respectively. Two 3D nano stages are used to realize the alignment of the sample on the gel film and the hole in the silicon substrate. Then, the gel film is brought into contact with the substrate and pressed gently. The sample is transferred to the hole area on the silicon substrate when the gel film is slowly moved away from the silicon substrate. The obtained suspended samples are identified by using an optical microscope, and an atomic force microscope (AFM) (NMAFM-2, Digital Instruments, CA, USA).

Experimental details

The Raman experiments are conducted by using a confocal Raman system, which is shown in Fig. 2(a). This system consists of a Raman spectrometer (Voyage, B&W Tek, Inc.) and a microscope (Olympus BX53). A CW laser (Excelsior, Spectra-Physics) or a ns laser (DCL AIO Laser, Photonics Industries, International, Inc.) with the same wavelength (532 nm) is introduced into the system, and a motorized neutral-density (ND) filter (CONEX-NSR, Newport Corporation) is used to adjust the laser power. The switch of the two lasers could be realized by a flip mirror without any other change to the system setup.

During the experiment, the Raman spectrometer and the ND filter are controlled by using a LabVIEW-based software program to realize automatic acquisition and saving of the Raman spectra, and automatic adjustment of the ND filter. At the same time, the experiment time is shortened significantly, the environmental interference to the system is reduced, and the accuracy of the experiment is improved dramatically. In the experiment, a 20× objective lens (NA = 0.4) is used for the two energy transport states. RSC of the sample under the two energy transport states could be obtained based on the acquired Raman spectra. For steady-state heating, the influence of hot carrier transfer on the measured RSC is much smaller when using the 20× objective lens than when using objective lens with a higher magnification. That is, the influence of hot carrier transfer is related to the laser spot size. The hot carrier diffusion length is around 0.4 μm for MoS_2, which is much smaller than the laser spot size under the 20× objective lens (around 3 μm).[21] As a result, the effect of hot carrier transfer becomes more negligible. For the transient-state heating, the energy density of the ns laser is very high. The larger the magnification of the objective lens, the higher the energy density of the laser on the sample. The sample will be damaged when the energy density is too high. As a result, the 20× objective lens is used. Then, RSC of the sample under the two energy transport states could be obtained based on the acquired Raman spectra to determine the in-plane thermal conductivity of the sample.

Conflicts of interest

There are no conflicts to declare.

Acknowledgements

The National Science Foundation (CBET1235852 and CMMI1264399) and the Department of Energy (DENE0000671) are gratefully acknowledged for the support of this work.

References

1 G. Fugallo, A. Cepellotti, L. Paulatto, M. Lazzeri, N. Marzari and F. Mauri, *Nano Lett.*, 2014, **14**, 6109–6114.

2 M. Han, P. Yuan, J. Liu, S. Si, X. Zhao, Y. Yue, X. Wang and X. Xiao, *Sci. Rep.*, 2017, **7**, 12213.

3 A. Gupta, T. Sakthivel and S. Seal, *Prog. Mater. Sci.*, 2015, **73**, 44–126.

4 X. Ling, S. Huang, E. H. Hasdeo, L. Liang, W. M. Parkin, Y. Tatsumi, A. R. Nugraha, A. A. Puretzky, P. M. Das, B. G. Sumpter, D. B. Geohegan, J. Kong, R. Saito, M. Drndic, V. Meunier and M. S. Dresselhaus, *Nano Lett.*, 2016, **16**, 2260–2267.

5 T. Wang, J. Liu, B. Xu, R. Wang, P. Yuan, M. Han, S. Xu, Y. Xie, Y. Wu and X. Wang, *ChemPhysChem*, 2017, **18**, 2828–2834.

6 R. Ganatra and Q. Zhang, *ACS Nano*, 2014, **8**, 4074–4099.

7 S. Larentis, B. Fallahazad and E. Tutuc, *Appl. Phys. Lett.*, 2012, **101**, 223104.

8 B. M. Nichols, A. L. Mazzoni, M. L. Chin, P. B. Shah, S. Najmaei, R. A. Burke and M. Dubey, *Semicond. Semimetals*, 2016, **95**, 221–277.

9 A. B. Kaul, *J. Mater. Res.*, 2014, **29**, 348–361.

10 E. Yalon, C. J. McClellan, K. K. H. Smithe, M. Munoz Rojo, R. L. Xu, S. V. Suryavanshi, A. J. Gabourie, C. M. Neumann, F. Xiong, A. B. Farimani and E. Pop, *Nano Lett.*, 2017, **17**, 3429–3433.

11 I. Jo, M. T. Pettes, J. Kim, K. Watanabe, T. Taniguchi, Z. Yao and L. Shi, *Nano Lett.*, 2013, **13**, 550–554.

12 H. Jang, J. D. Wood, C. R. Ryder, M. C. Hersam and D. G. Cahill, *Adv. Mater.*, 2015, **27**, 8017–8022.

13 A. Aiyiti, X. Bai, J. Wu, X. Xu and B. Li, *Sci. Bull.*, 2018, **63**(7), 452–458.

14 K. M. Shahil and A. A. Balandin, *Nano Lett.*, 2012, **12**, 861–867.

15 D. Zhao, X. Qian, X. Gu, S. A. Jajja and R. Yang, *J. Electron. Packag.*, 2016, **138**, 040802.

16 J.-U. Lee, M. Kim and H. Cheong, *Appl. Microsc.*, 2015, **45**, 126–130.

17 S. Najmaei, Z. Liu, P. M. Ajayan and J. Lou, *Appl. Phys. Lett.*, 2012, **100**, 013106.

18 L. Su and Y. Zhang, *Appl. Phys. Lett.*, 2015, **107**, 071905.

19 H.-D. Wang, J.-H. Liu, X. Zhang and Y. Song, *Int. J. Heat Mass Transfer*, 2014, **70**, 40–45.

20 A. Aiyiti, S. Hu, C. Wang, Q. Xi, Z. Cheng, M. Xia, Y. Ma, J. Wu, J. Guo, Q. Wang, J. Zhou, J. Chen, X. Xu and B. Li, *Nanoscale*, 2018, **10**, 2727–2734.

21 P. Yuan, J. Liu, R. Wang and X. Wang, *Nanoscale*, 2017, **9**, 6808–6820.

22 J.-U. Lee, D. Yoon, H. Kim, S. W. Lee and H. Cheong, *Phys. Rev. B: Condens. Matter*, 2011, **83**, 081419.

23 Z. Luo, J. Maassen, Y. Deng, Y. Du, R. P. Garrelts, M. S. Lundstrom, P. D. Ye and X. Xu, *Nat. Commun.*, 2015, **6**, 8572.

24 R. Yan, J. R. Simpson, S. Bertolazzi, J. Brivio, M. Watson, X. Wu, A. Kis, T. Luo, A. R. H. Walker and H. G. Xing, *ACS Nano*, 2014, **8**, 986–993.

25 X. Zhang, D. Sun, Y. Li, G. H. Lee, X. Cui, D. Chenet, Y. You, T. F. Heinz and J. C. Hone, *ACS Appl. Mater. Interfaces*, 2015, **7**, 25923–25929.

26 P. Yuan, R. Wang, H. Tan, T. Wang and X. Wang, *ACS Photonics*, 2017, **4**, 3115–3129.

27 D. J. Late, S. N. Shirodkar, U. V. Waghmare, V. P. Dravid and C. N. Rao, *ChemPhysChem*, 2014, **15**, 1592–1598.

28 S. Sahoo, A. P. S. Gaur, M. Ahmadi, M. J. F. Guinel and R. S. Katiyar, *J. Phys. Chem. C*, 2013, **117**, 9042–9047.
29 X. Chen and X. Wang, *J. Phys. Chem. C*, 2011, **115**, 22207–22216.
30 C. Yim, M. O'Brien, N. McEvoy, S. Winters, I. Mirza, J. G. Lunney and G. S. Duesberg, *Appl. Phys. Lett.*, 2014, **104**, 103114.
31 H.-L. Liu, C.-C. Shen, S.-H. Su, C.-L. Hsu, M.-Y. Li and L.-J. Li, *Appl. Phys. Lett.*, 2014, **105**, 201905.
32 C. Christofides, A. Othonos and E. Loizidou, *J. Appl. Phys.*, 2002, **92**, 1280–1285.
33 E. Marin, *Lat.-Am. J. Phys. Educ.*, 2010, **4**, 5.
34 S. Sinha, *Ceram. Int.*, 2015, **41**, 6596–6603.
35 S. K. Balasingam, J. S. Lee and Y. Jun, *Dalton Trans.*, 2015, **44**, 15491–15498.
36 H. Li, J. Wu, Z. Yin and H. Zhang, *Acc. Chem. Res.*, 2014, **47**, 1067–1075.
37 A. Castellanos-Gomez, M. Buscema, R. Molenaar, V. Singh, L. Janssen, H. S. J. van der Zant and G. A. Steele, *2D Mater.*, 2014, **1**, 011002.
38 E. Mercado, A. Goodyear, J. Moffat, M. Cooke and R. S. Sundaram, *J. Phys. D: Appl. Phys.*, 2017, **50**, 184005.
39 E. Pop, V. Varshney and A. K. Roy, *MRS Bull.*, 2012, **37**, 1273–1281.
40 B. Qiu and X. Ruan, *Appl. Phys. Lett.*, 2012, **100**, 193101.
41 J. J. Bae, H. Y. Jeong, G. H. Han, J. Kim, H. Kim, M. S. Kim, B. H. Moon, S. C. Lim and Y. H. Lee, *Nanoscale*, 2017, **9**, 2541–2547.
42 I. Jo, M. T. Pettes, E. Ou, W. Wu and L. Shi, *Appl. Phys. Lett.*, 2014, **104**, 201902.
43 A. Taube, J. Judek, A. Lapinska and M. Zdrojek, *ACS Appl. Mater. Interfaces*, 2015, **7**, 5061–5065.
44 Y. Cai, J. Lan, G. Zhang and Y.-W. Zhang, *Phys. Rev. B: Condens. Matter*, 2014, **89**, 035438.
45 T. S. Sreeprasad, P. Nguyen, N. Kim and V. Berry, *Nano Lett.*, 2013, **13**, 4434–4441.
46 J. Liu, G.-M. Choi and D. G. Cahill, *J. Appl. Phys.*, 2014, **116**, 233107.
47 Y. Hong, J. Zhang and X. C. Zeng, *J. Phys. Chem. C*, 2016, **120**, 26067–26075.
48 B. Peng, H. Zhang, H. Shao, Y. Xu, X. Zhang and H. ZHu, *RSC Adv.*, 2016, **6**, 5767–5773.
49 P. Jiang, X. Qian, X. Gu and R. Yang, *Adv. Mater.*, 2017, **29**, 1701068.
50 X. Gu, B. Li and R. Yang, *J. Appl. Phys.*, 2016, **119**, 085106.
51 M. T. Pettes, J. Maassen, I. Jo, M. S. Lundstrom and L. Shi, *Nano Lett.*, 2013, **13**, 5316–5322.
52 C. Jeong, S. Datta and M. Lundstrom, *J. Appl. Phys.*, 2012, **111**, 093708.